

## Time-resolved photoelectron imaging spectra from non-adiabatic molecular dynamics simulations

Alexander Humeniuk, Matthias Wohlgemuth, Toshinori Suzuki, and Roland Mitri

Citation: *The Journal of Chemical Physics* **139**, 134104 (2013); doi: 10.1063/1.4820238

View online: <http://dx.doi.org/10.1063/1.4820238>

View Table of Contents: <http://scitation.aip.org/content/aip/journal/jcp/139/13?ver=pdfcov>

Published by the [AIP Publishing](#)

---

### Articles you may be interested in

[Following the relaxation dynamics of photoexcited aniline in the 273-266 nm region using time-resolved photoelectron imaging](#)

*J. Chem. Phys.* **139**, 034316 (2013); 10.1063/1.4813005

[Study of ultrafast dynamics of 2-picoline by time-resolved photoelectron imaging](#)

*J. Chem. Phys.* **134**, 234301 (2011); 10.1063/1.3600334

[Simulation of time resolved photoelectron spectra with Stieltjes imaging illustrated on ultrafast internal conversion in pyrazine](#)

*J. Chem. Phys.* **132**, 174301 (2010); 10.1063/1.3395160

[Nonadiabatic dynamics and simulation of time resolved photoelectron spectra within time-dependent density functional theory: Ultrafast photoswitching in benzylideneaniline](#)

*J. Chem. Phys.* **129**, 164118 (2008); 10.1063/1.3000012

[Real-time observation of intramolecular proton transfer in the electronic ground state of chloromalonaldehyde: An ab initio study of time-resolved photoelectron spectra](#)

*J. Chem. Phys.* **126**, 054303 (2007); 10.1063/1.2432119

---



## Re-register for Table of Content Alerts

Create a profile.



Sign up today!



# Time-resolved photoelectron imaging spectra from non-adiabatic molecular dynamics simulations

Alexander Humeniuk,<sup>1</sup> Matthias Wohlgenuth,<sup>2</sup> Toshinori Suzuki,<sup>3</sup> and Roland Mitrić<sup>1,2,a)</sup>

<sup>1</sup>Fachbereich Physik, Freie Universität Berlin, Arnimallee 14, 14195 Berlin, Germany

<sup>2</sup>Institut für Physikalische und Theoretische Chemie, Julius-Maximilians Universität Würzburg, Emil-Fischer-Straße 42, 97074 Würzburg, Germany

<sup>3</sup>Department of Chemistry, Graduate School of Science, Kyoto University, Kyoto 606-8502, Japan; RIKEN Center for Advanced Photonics, RIKEN, Wako, Saitama 351-0198, Japan; CREST, Japan Science and Technology Agency, Sanbancho, Chiyoda-ku, Tokyo 102-0075, Japan

(Received 29 April 2013; accepted 21 August 2013; published online 2 October 2013)

We present an efficient method for the simulation of time-resolved photoelectron imaging (TRPEI) spectra in polyatomic molecules. Our approach combines trajectory-based molecular dynamics that account for non-adiabatic effects using surface hopping, with an approximate treatment of the photoionization process using Dyson orbitals as initial and Coulomb waves as final electron states. The method has been implemented in the frame of linear response time-dependent density functional theory. As an illustration, we simulate time- and energy-resolved anisotropy maps for the furan molecule and compare them with recent experimental data [T. Fuji, Y.-I. Suzuki, T. Horio, T. Suzuki, R. Mitrić, U. Werner, and V. Bonačić-Koutecký, *J. Chem. Phys.* **133**, 234303 (2010)]. Our method can be generally used for the interpretation of TRPEI experiments allowing to shed light into the fundamental photochemical processes in complex molecules. © 2013 AIP Publishing LLC. [<http://dx.doi.org/10.1063/1.4820238>]

## I. INTRODUCTION

In polyatomic molecules the dynamics of electrons and nuclei are often coupled in an intricate way giving rise to fundamental photochemical processes such as internal conversion or intersystem crossing.<sup>2</sup> These processes govern the fate of the electronically excited molecules and represent fundamental steps involved in photochemical reactions, biological processes such as vision,<sup>3</sup> stabilization of DNA against UV-radiation<sup>4</sup> or light harvesting and numerous technological applications.

A powerful experimental tool for studying non-adiabatic dynamics in excited states and non-radiative transitions is time- and angle-resolved photoelectron imaging (TRPEI).<sup>5–8</sup> In short, in TRPEI experiments first an ultrafast pump pulse creates a wave packet on an excited electronic state. Then the system is allowed to evolve freely, moving on the excited state potential energy surfaces and undergoing non-radiative transitions to other states. After some time-delay a probe pulse ionizes the molecule and the intensity of the ejected electrons is measured as a function of the angle and photoelectron kinetic energy (PKE). By repeating the experiment with different time delays, the dynamics can be mapped to a time-sequence of observables. A map of the anisotropy of the signal reveals ultrafast non-radiative transitions<sup>7–11</sup> because these often cause the electronic character of the wave function to change abruptly.

The simulation of these non-adiabatic effects still poses challenges to current theory, since it requires an accurate description of the electronic structure of the involved molecules,

their quantum dynamics, and the electronic continuum to which the photoelectron is ionized. Previously, nuclear wave packets have been propagated on globally precalculated potential energy surfaces and femtosecond time-resolved photoelectron spectra and photoelectron angular distributions have been simulated using the Lippmann-Schwinger equations to obtain photoionization matrix elements.<sup>12,13</sup> The same authors developed a variational principle that allows to calculate the transition dipole moments between bound and continuum states iteratively on the basis of atomic centered orbitals. The application of this method to NO<sub>2</sub> has shown that although the contribution from different non-radiative channels cannot be distinguished in the time-resolved photoelectron spectrum alone, the angular resolved photoelectron distributions allow to track the wave packet dynamics near the conical intersections.<sup>13</sup> Since the exact wave packet propagation is limited to systems with a small number of nuclear degrees of freedom, it is highly desirable to develop methods for the simulation of TRPEI spectra utilizing more approximate propagation methods which are generally applicable to polyatomic molecules. In this context, previously the time-resolved photoelectron spectra for several systems have been calculated in the framework of the *ab initio* multiple spawning (AIMS)<sup>14,15</sup> as well as trajectory surface hopping methods.<sup>16,17</sup>

The aim of this paper is to extend the existing methodology to efficient simulations of both time-, energy- as well as angle-resolved photoelectron spectra in polyatomic molecules in the gas phase allowing for the full interpretation of recent TRPEI experiments.<sup>1,7,9–11</sup> Our approach combines the surface hopping non-adiabatic dynamics “on the fly” with an approximate treatment of photoionization using Fermi’s

<sup>a)</sup> Author to whom correspondence should be addressed. Electronic mail: roland.mitric@uni-wuerzburg.de

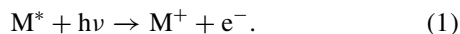
golden rule and Dyson orbitals<sup>19</sup> calculated along classical non-adiabatic trajectories.

The paper is structured as follows: In Sec. II we describe how we model the photoionization process, we give working equations for computing anisotropies (Sec. II A) and describe the procedure for calculating Dyson orbitals (Sec. II B) within linear response time-dependent density functional theory (TDDFT). Furthermore, we discuss different approximations for the scattering states (Sec. II C) representing the ionized system. In Sec. III we apply the simulation procedure to furan and explain how anisotropy maps are generated from Dyson orbitals along non-adiabatic trajectories. Finally, in Sec. III B we analyze our dynamics simulation and compare with experimental data on furan.

## II. THEORY

### A. Theoretical description of photoionization along non-adiabatic trajectories

Since the photoionization process is much faster than the motion of the nuclei, we can assume that the nuclear geometry  $\vec{R}(t)$ , representing a configuration along a non-adiabatic trajectory, remains constant while the electron is ejected. If the intensity of the ionizing radiation is chosen low enough to avoid multiple ionization and the probe pulse has Gaussian shape, the transition probability to the continuum can be approximately calculated using Fermi's golden rule.<sup>20</sup> In photoionization of a polyatomic molecule, the initial and final states are multielectron states consisting initially of an electronically excited molecule with a bound electron that interacts with a photon to give an ion and a free electron:



By noting that the molecule interacts with light through coupling to the dipole operator, which is a single particle operator, the interaction can be reduced to a single particle process: The initial state is a single electron in an effective orbital  $\psi^D$ , called Dyson orbital<sup>5,6,21,22</sup> (see Sec. II B below), while the final state  $\psi_k^{(-)}$  is a scattering state of the ionized molecule (see Sec. II C) that asymptotically has linear momentum  $\vec{k}$ . The differential cross section for the photoionization according to Fermi's golden rule is given by

$$\frac{d\sigma}{d\Omega} \propto |\langle \psi_k^{(-)} | \vec{E} \cdot \vec{r} | \psi^D \rangle|^2. \quad (2)$$

Notice that field polarization and electron momentum are vectors defined in the laboratory frame, while the Dyson orbital and the continuum orbital are defined in the molecular frame. Thus, one frame has to be rotated into the other by a rotation matrix  $\mathbf{R}$  in order to calculate the above matrix element (Eq. (2)).

We assume that initially all molecules are isotropically oriented and reside in the ground state. A linearly polarized pump pulse preferentially excites those molecules whose transition dipole moment  $\vec{d}_{0 \rightarrow I}$  between the ground state and the state that is resonantly pumped is aligned with the polarization vector  $\vec{E}$ . To first order, the transition probability depends on

the cosine of the angle between the two vectors:

$$T_{0 \rightarrow I} \propto |\langle \Psi_I | \vec{E} \cdot \vec{r} | \Psi_0 \rangle|^2 \propto \cos^2(\angle(\vec{E}, \vec{d}_{0 \rightarrow I})), \quad (3)$$

which leads to an excited state population with aligned dipole moments. During time delays between pump and probe pulse that are shorter than the rotational period, the molecules cannot reorient. The probe pulse therefore encounters an aligned ensemble in the excited state that can be characterized by a distribution of orientations  $f(\mathbf{R})$ .

Each molecular orientation corresponds to a rotation around three Euler angles  $(\alpha, \beta, \gamma)$ . Molecules with orientation given by the rotation matrix  $\mathbf{R}_{\vec{d} \rightarrow \hat{z}} = \mathbf{R}(\alpha, \beta, \gamma)$ , that rotates the transition dipole moment  $\vec{d}$  into the z-axis, will be selected by the pump pulse. The spherical coordinates of the transition dipole are related to the Euler angles of the most likely orientation:

$$\vec{d} = |\vec{d}| \begin{pmatrix} \sin(\Theta) \cos(\Phi) \\ \sin(\Theta) \sin(\Phi) \\ \cos(\Theta) \end{pmatrix} \Rightarrow \begin{matrix} \alpha_d = \text{arbitrary} \\ \beta_d = \Theta \\ \gamma_d = \pi - \Phi \end{matrix}. \quad (4)$$

As both pump and probe pulse are linearly polarized and parallel to the z-axis, the distribution  $f$  only depends on the angle  $\beta - \Theta$  (how much does the angle deviate from the perfectly aligned transition dipole moment). For an ensemble that has been aligned by pumping with a beam polarized along the z-axis, the orientations are, therefore, distributed around the angle  $\Theta = \angle(\vec{E}, \vec{d}_{0 \rightarrow I})$  between the transition dipole moment and the polarization vector according to

$$f_{\text{aligned}}(\mathbf{R}) = \frac{3}{2} \cos^2(\beta(\mathbf{R}) - \Theta). \quad (5)$$

In order to calculate the photoionization cross section, averaging over molecular orientations weighted by the distribution given in Eq. (5) needs to be performed:

$$\overline{\frac{d\sigma}{d\Omega}} \propto \int d\mathbf{R} \langle |\psi_{\mathbf{R}\vec{k}}^{(-)} | \vec{E} \cdot (\mathbf{R}^{-1}\vec{r}) | \psi^D \rangle|^2 f(\mathbf{R}). \quad (6)$$

The averaged scattering cross section depends only on the angle  $\theta_k$  between the polarization vector (or the z-axis for light circularly polarized in the xy-plane) and the electron momentum and can be characterized for non-chiral molecules by two quantities, the total scattering cross section  $\sigma$  and the anisotropy  $\beta$  (ranging between  $-1.0$  and  $2.0$ ):

$$\overline{\frac{d\sigma}{d\Omega}} = \frac{\sigma}{4\pi} [1 + \beta P_2(\cos(\theta_k))], \quad (7)$$

where  $P_2(x)$  is the second Legendre polynomial.<sup>23</sup> A TRPEI experiment is fully described by maps of these two parameters in the time and photoelectron kinetic energy domain. For prealigned molecules the averaged cross section can also depend on higher even powers of  $\cos(\theta_k)$  but these are usually small.

To find analytical expressions for  $\sigma$  and  $\beta$  the dipole interaction with a polarized electric field  $\vec{E}_{m_p}$  ( $m_p = 0, -1, 1$  stands for a linearly, left and right-polarized probe pulse) and the initial and final states  $\psi^D$  and  $\psi^{(-)}$  are expanded into

spherical harmonics with respect to  $\vec{r}$  and  $\vec{k}$ :

$$\vec{E}_{m_p} \cdot (\mathbf{R}^{-1}\vec{r}) = |\vec{E}| (1 - 2\delta_{1,m_p}) \sqrt{\frac{4\pi}{3}} r \times \sum_{m'=-1,0,1} D_{m',m_p}^1(\mathbf{R}^{-1}) Y_{1,m'}(\hat{r}), \quad (8)$$

$$\psi^D(\vec{r}) = \sum_{l_y=0}^{\infty} \sum_{m_y=-l_y}^{l_y} \psi_{l_y,m_y}^D(r) Y_{l_y,m_y}(\hat{r}), \quad (9)$$

$$\psi^{(-)}(\vec{r}, \mathbf{R} \cdot \vec{k}) = \sum_{l_r=0}^{\infty} \sum_{m_r=-l_r}^{l_r} \sum_{l_k=0}^{\infty} \sum_{m_k=-l_k}^{l_k} \psi_{l_r,m_r;l_k,m_k}^{(-)}(r, k) \times Y_{l_r,m_r}(\hat{r}) Y_{l_k,m_k}^*(\mathbf{R} \cdot \vec{k}). \quad (10)$$

Now the average in Eq. (6) can be performed in part analytically using the transformation properties of spherical harmonics under rotations and formulae for averages over Wigner D-matrices.<sup>24</sup> In one of the intermediate steps one has to integrate products of Wigner D-matrices over Euler angles weighted with the distribution function to obtain an orientation factor (*OF*) that accounts for the orientation distribution:

$$\text{OF} = \frac{1}{8\pi^2} \int_0^{2\pi} d\alpha \int_0^\pi \sin(\beta) d\beta \int_0^{2\pi} d\gamma f(\alpha, \beta, \gamma) \times D_{0,m_1-m_2}^{l_1*}(\alpha, \beta, \gamma) D_{m_k,m_\delta-m_\beta}^{l_2}(\alpha, \beta, \gamma). \quad (11)$$

The  $\alpha$ - and  $\gamma$ -integrals can be performed analytically:

$$\begin{aligned} \text{OF}[f(\alpha, \beta, \gamma) = f(\beta)] &= \frac{1}{8\pi^2} \int_0^{2\pi} d\alpha \int_0^{2\pi} d\gamma e^{im_k\alpha} e^{i(m_\delta-m_\beta-m_1+m_2)\gamma} \int_0^\pi \sin(\beta) d\beta d_{0,m_1-m_2}^{l_1}(\beta) \times d_{m_k,m_\delta-m_\beta}^{l_2}(\beta) f(\beta - \Theta) d\beta \\ &= \frac{1}{2} \delta_{m_k,0} \delta_{m_\delta-m_\beta,m_1-m_2} \int_0^\pi \sin(\beta) d_{0,m_1-m_2}^{l_1}(\beta) \times d_{m_k,m_\delta-m_\beta}^{l_2}(\beta) f(\beta - \Theta) d\beta. \end{aligned} \quad (12)$$

Here  $d_{m',m}^{l'}(\beta)$  are the small Wigner-D matrices (see Eq. (4.5.2) in Ref. 24). The remaining one-dimensional integral over  $\beta$  can be calculated easily by numerical quadrature. The orientation averaged photoionization cross section from an aligned ensemble thus becomes

$$\begin{aligned} &\left( \frac{d\sigma^{m_p}}{d\Omega}(\theta_k) \right)_{\text{aligned}} \\ &= \alpha \left( \frac{k^2}{2} + \text{IE} \right) k \sum_{l_1=0}^2 \frac{2l_1+1}{4\pi} \begin{pmatrix} 1 & 1 & l_1 \\ -m_p & m_p & 0 \end{pmatrix} \\ &\times \sum_{m_1=-1,0,1} \sum_{m_2=-1,0,1} \begin{pmatrix} 1 & 1 & l_1 \\ -m_2 & m_1 & m_2 - m_1 \end{pmatrix} \end{aligned}$$

$$\begin{aligned} &\times \sum_{l_\beta=0}^{\infty} \sum_{l_\delta=0}^{\infty} \sum_{l_2=|l_\beta-l_\delta|}^{l_\beta+l_\delta} \\ &\times \int_0^\pi \sin(\beta) d_{0,m_1-m_2}^{l_1}(\beta) d_{0,m_1-m_2}^{l_2}(\beta) f(\beta - \Theta) d\beta \\ &\times (2l_2+1) \begin{pmatrix} l_\beta & l_\delta & l_2 \\ 0 & 0 & 0 \end{pmatrix} \\ &\times \sum_{m_\beta=-l_\beta}^{l_\beta} \sum_{m_\delta=-l_\delta}^{l_\delta} (-1)^{m_1+m_p+m_\delta} \sqrt{(2l_\beta+1)(2l_\delta+1)} \\ &\times \begin{pmatrix} l_\beta & l_\delta & l_2 \\ -m_\beta & m_\delta & m_2 - m_1 \end{pmatrix} \\ &\times \delta_{m_\delta-m_\beta,m_1-m_2} \times \tilde{I}_{l_\beta,m_\beta,m_1}(k) \tilde{I}_{l_\delta,m_\delta,m_2}^*(k) P_{l_2}(\cos(\theta_k)). \end{aligned} \quad (13)$$

In this expression  $\sigma$  equals the terms linear in  $P_0$  and  $\beta$  equals the terms linear in  $P_2$  divided by  $\sigma/4\pi$ . The terms  $\tilde{I}_{l_\beta,m_\beta,m_1}(k)$  are defined as

$$\begin{aligned} &\tilde{I}_{l_\beta,m_\beta,m_1}(k) \\ &= \sqrt{\frac{2}{\pi}} \left\{ (-1)^{m_1} \frac{1}{\sqrt{3}} \int r^3 \psi_{0,0}^{D*}(r) \psi_{1,-m_1;l_\beta,m_\beta}^{(-)}(r, k) dr \right. \\ &+ \sum_{l_\gamma=1}^{\infty} \sum_{m_\gamma=-l_\gamma}^{l_\gamma} (-1)^{l_\gamma+m_\gamma} \left[ \sqrt{l_\gamma} \begin{pmatrix} l_\gamma - 1 & 1 & l_\gamma \\ m_\gamma - m_1 & m_1 & -m_\gamma \end{pmatrix} \right. \\ &\times \int r^3 \psi_{l_\gamma,m_\gamma}^{D*}(r) \psi_{l_\gamma-1,m_\gamma-m_1;l_\beta,m_\beta}^{(-)}(r, k) dr \\ &- \sqrt{l_\gamma+1} \begin{pmatrix} l_\gamma & 1 & l_\gamma+1 \\ -m_\gamma & m_1 & m_\gamma - m_1 \end{pmatrix} \\ &\left. \left. \times \int r^3 \psi_{l_\gamma,m_\gamma}^{D*}(r) \psi_{l_\gamma+1,m_\gamma-m_1;l_\beta,m_\beta}^{(-)}(r, k) dr \right] \right\}. \end{aligned} \quad (14)$$

This expression shows that the cross section involves overlaps between partial waves of the Dyson orbital with angular momentum  $l_\gamma$  (i.e.,  $\psi_{l_\gamma,m_\gamma}^{D*}$ ) and partial waves of the continuum state with angular momenta  $l_\gamma+1$  and  $l_\gamma-1$  (i.e.,  $\psi_{l_\gamma+1,m_\gamma-m_1;l_\beta,m_\beta}^{(-)}$  and  $\psi_{l_\gamma-1,m_\gamma-m_1;l_\beta,m_\beta}^{(-)}$ ).

To check the consistency of our formulae we consider resonant photoionization from an isotropically oriented ensemble. For an isotropic distribution of orientations we have  $f_{\text{iso}}(\beta) = \frac{1}{2}$  and Eq. (13) reduces to the expressions for the averaged photoelectron angular distribution derived in Ref. 25 or in the appendix of Ref. 26.

## B. Dyson orbitals within linear response TDDFT

The Dyson orbital is a single electron wave function defined as the overlap between the neutral state with  $N$  electrons and the cationic state with  $N-1$  electrons

$$|\phi^D\rangle = \sqrt{N} \langle \Phi^{N-1} | \Phi^N \rangle, \quad (15)$$

where the integration is performed over  $N-1$  electrons so that the transition dipole integral has the form

$$\langle \vec{k} | \otimes \langle \Phi^{N-1} | \sum_{i=1}^N \vec{E} \cdot \vec{r}_i | \Phi^N \rangle = \langle \vec{k} | \vec{E} \cdot \vec{r} | \Phi^D \rangle. \quad (16)$$

Since the integration only extends over the coordinates of  $N-1$  electrons, the Dyson orbital has still a dependence on one electron coordinate and represents the effective single particle orbital from which the electron is ionized in the approximation that the electron does not interact with the cationic core. It also takes into account the electronic reconfiguration between the neutral molecule and the ion.

In our case, the Dyson orbitals depend parametrically on a non-adiabatic nuclear trajectory  $\vec{R}(t)$  and since the ionization takes place on a much shorter time scale than the movement of the nuclei, we calculate the ground- and excited states of the neutral and ionized molecule at the same geometry.

Although linear response TDDFT operates with the electron density, wave functions can be assigned to excited states on the basis of TDDFT linear response eigenvectors.<sup>27</sup> The wave function of the  $i$ th excited state is represented as a linear combination of single excitations from the Kohn-Sham reference determinant  $|\Phi_0^N\rangle$  (containing  $N$  electrons):

$$|\Phi_i^N\rangle = \sum_{\substack{o \in \text{occupied} \\ v \in \text{virtual}}} c_{o,v}^i a_v^\dagger a_o |\Phi_0^N\rangle, \quad (17)$$

with the weights  $c_{o,v}^i$  where  $o$  and  $v$  stand for occupied and virtual spin orbitals with the same spin. The Dyson orbital for the transition from a neutral to a cation state will then be a linear combination of overlaps between singly excited determinants with  $N$  and with  $N-1$  electrons.

The Kohn-Sham orbitals of the neutral molecule will in general differ from those of the ionized molecule, so that one needs rules for the computation of overlaps between Slater determinants built from different sets of molecular orbitals. In the following  $|\Psi^N\rangle$  and  $|\Psi^{N-1}\rangle$  will denote Slater determinants built from the neutral set of molecular orbitals  $\{\phi_1(x), \dots, \phi_N(x)\}$  and the cationic set  $\{\chi_1(x), \dots, \chi_{N-1}(x)\}$ , respectively. A neutral determinant can be written as

$$\Psi^N(x_1, \dots, x_N) = \langle x_1, \dots, x_N | \{\phi_1, \phi_2, \dots, \phi_N\} \rangle = \sqrt{\frac{1}{N!}} \begin{vmatrix} \phi_1(x_1) & \phi_2(x_1) & \dots & \phi_N(x_1) \\ \phi_1(x_2) & \phi_2(x_2) & \dots & \phi_N(x_2) \\ \vdots & \vdots & \ddots & \vdots \\ \phi_1(x_N) & \phi_2(x_N) & \dots & \phi_N(x_N) \end{vmatrix}. \quad (18)$$

The determinant can be expanded in the last row to give a sum over Slater determinants of dimension  $N-1$ . Note that the  $i$ th orbital is missing from the  $i$ th Slater determinant and that the minor determinants are functions of the first  $N-1$  electron positions only:

$$\langle x_N | \Psi^N \rangle = \sqrt{\frac{(N-1)!}{N!}} \sum_{i=1}^N (-1)^{i+1} \times |\{\phi_1, \dots, \phi_{i-1}, \phi_{i+1}, \dots, \phi_N\}\rangle \phi_i(x_N). \quad (19)$$

Overlapping with an  $N-1$  electron Slater determinant yields the Dyson orbital between a neutral and a cationic Slater determinant:

$$\phi_{\text{Slater}}^D(x) = \sqrt{N} \int \Psi^{N-1}(x_1, x_2, \dots, x_{N-1})^* \Psi^N(x_1, x_2, \dots, x_{N-1}, x) dx_1 dx_2 \dots dx_{N-1}, \quad (20)$$

$$= \sum_{i=1}^N (-1)^{i+1} \langle \{\chi_1, \chi_2, \dots, \chi_{N-1}\} | \{\phi_1, \dots, \phi_{i-1}, \phi_{i+1}, \dots, \phi_N\} \rangle \phi_i(x). \quad (21)$$

This equation can be written in the symbolic form

$$|\phi_{\text{Slater}}^D\rangle = \begin{vmatrix} \langle \chi_1 | \phi_1 \rangle & \langle \chi_1 | \phi_2 \rangle & \dots & \langle \chi_1 | \phi_N \rangle \\ \langle \chi_2 | \phi_1 \rangle & \langle \chi_2 | \phi_2 \rangle & \dots & \langle \chi_2 | \phi_N \rangle \\ \vdots & \vdots & \ddots & \vdots \\ \langle \chi_{N-1} | \phi_1 \rangle & \langle \chi_{N-1} | \phi_2 \rangle & \dots & \langle \chi_{N-1} | \phi_N \rangle \\ |\phi_1\rangle & |\phi_2\rangle & \dots & |\phi_N\rangle \end{vmatrix}, \quad (22)$$

which only makes sense, if the determinant is expanded along the last row, which contains the molecular orbitals of the neutral molecule.

As the nuclear geometry remains fixed during the ionization, the same atomic basis set  $\{a_1(x), a_2(x), \dots, a_K(x)\}$  can be employed to represent the neutral and cationic molecular

orbitals:

$$|\phi_j\rangle = \sum_{\mu=1}^K C_{\mu j}^N a_\mu(x), \quad (23)$$

$$|\chi_j\rangle = \sum_{v=1}^K C_{v j}^{N-1} a_v(x), \quad (24)$$

where  $C_{\mu j}^N$  and  $C_{v j}^{N-1}$  are the molecular orbital expansion coefficients for the neutral and the ionized molecules, respectively. Denoting the overlap matrix between the atomic orbitals by  $S_{v\mu} = \int a_v^*(x) a_\mu(x) dx$ , the overlaps between the neutral and the cationic molecular orbitals become

$$\langle \chi_i | \phi_j \rangle = \sum_{\mu=1}^K \sum_{v=1}^K (C_{vi}^{N-1})^* C_{\mu j}^N S_{v\mu}. \quad (25)$$

If the Kohn-Sham orbitals for the neutral and ionized molecule do not differ greatly and if, furthermore, the excited states are dominated by a single electronic configuration, then the Dyson orbital will just be the molecular orbital that is not occupied in both the neutral and the ionized molecule. On the other hand, if electron correlations play a major role, then the Dyson orbital may deviate from the individual molecular orbitals. The norm of the Dyson orbital indicates the strength of the photoionization signal. If the norm is sufficiently low, the particular transition can be neglected in the analysis.

### C. Approximate description of the continuum states

Description of photoionization requires the solution of a scattering problem, which is computationally very demanding for molecules with many degrees of freedom. Calculation of molecular scattering states are still not part of standard quantum chemical methodology. For fixed ground state geometries the ionization parameters have been calculated by combining configuration interaction methods for bound states and continuum multiple scattering  $X\alpha$  methods for continuum states.<sup>40</sup> Since our aim is the description of dynamical evolution of photoelectron spectra, we need to calculate scattering states very often along non-adiabatic nuclear trajectories. For this purpose we adopt two different alternative approximations introduced in Ref. 22 for the final continuum states: For photodetachment of an electron from an anion one can assume that the continuum states are free plane waves  $e^{i\vec{k}\cdot\vec{r}}$ , for which the spherical wave expansion (Eq. (10)) with respect to  $\hat{r}$  and  $\hat{k}$  reads<sup>28</sup>

$$\psi_{l_\alpha, m_\alpha; l_\beta, m_\beta}^{(-)}(r, k) = 4\pi i^{l_\alpha} j_{l_\alpha}(kr) \delta_{l_\alpha, l_\beta} \delta_{m_\alpha, m_\beta}, \quad (26)$$

where  $j_n(x)$  are the spherical Bessel functions of the first kind.<sup>29,30</sup> If a neutral molecule is ionized, the Coulomb potential generated by the positive charge of the remaining cation, acts over a long range. For photoionization from neutral molecules the continuum states can be better approximated by the scattering states of the Coulomb potential,<sup>31</sup> whose spherical wave decomposition with respect to  $\hat{r}$  and  $\hat{k}$  is<sup>32</sup>

$$\psi_{l_\alpha, m_\alpha; l_\beta, m_\beta}^{(-)}(r, k) = 4\pi i^{l_\alpha} e^{i\sigma_l} \times \frac{1}{kr} F_{l_\alpha} \left( -\frac{1}{k}, kr \right) \delta_{l_\alpha, l_\beta} \delta_{m_\alpha, m_\beta}. \quad (27)$$

Here  $F_l(\eta, \rho)$  is the regular Coulomb function and  $\sigma_l = \arg\Gamma(l + 1 - iZ/k)$  are the Coulomb phase shifts. While Coulomb waves are the exact scattering states of a Coulomb potential, for general molecules neither Coulomb nor Bessel functions represent the correct scattering states. Asymptotically the scattering states will coincide either with linear combinations of Bessel functions or Coulomb waves depending on whether the molecule is neutrally or positively charged after the removal of one electron. For molecules, the correct scattering states are as complex as their bound states. Approximating them by spherically symmetric scattering states of hydrogen is a very drastic simplification especially at photoelectron kinetic energies closely above the ionization threshold. At high photoelectron kinetic energies the approximations might be more warranted, since

in the Schrödinger equation the molecular potential can be neglected as compared with the large eigenenergy.

These simple approximations can be improved by orthogonalizing the final continuum state with respect to the Dyson orbital.<sup>19</sup> Formally this can be achieved by subtracting from the final state its projection along the initial state and normalizing the result. If the final state with momentum  $\vec{k}$  is denoted by  $|k\rangle$ , the orthogonal not yet normalized state becomes

$$|\tilde{k}\rangle = |k\rangle - \langle\psi^D|k\rangle|\psi^D\rangle. \quad (28)$$

Instead of calculating the overlap  $\langle\psi^D|k\rangle$  the same results can be reached by shifting the origin of the coordinate system, so that the expectation value of the dipole operator in the Dyson orbital vanishes. Then the transition dipole moments, from which the cross section is computed, are the same regardless of whether the orthogonal or the unmodified final states are used:

$$\langle\psi^D|\vec{r}|\tilde{k}\rangle = \langle\psi^D|\vec{r}|k\rangle - \langle\psi^D|k\rangle \underbrace{\langle\psi^D|\vec{r}|\psi^D\rangle}_0. \quad (29)$$

## III. TRPEI OF FURAN

### A. Computational details

#### 1. Electronic structure of furan

As discussed previously,<sup>1</sup> the electronic structure of furan has been described at the TDDFT level using the hybrid PBE0 functional<sup>33</sup> together with the 6-311++G\*\* atomic basis set.<sup>34</sup> At the planar equilibrium geometry the spectrum of furan exhibits a dark first excited state  $S_1$  ( $\epsilon_1 = 5.87$  eV) with Rydberg character and a bright second excited state  $S_2$  ( $\epsilon_2 = 6.21$  eV) with  $\pi - \pi^*$  character (cf. Fig. 1).

The initial ensemble for the dynamics simulations has been obtained by sampling 189 uncorrelated initial positions and velocities from a 20 ps ground state trajectory at 300 K.

Since the experimental pump pulse of 6.2 eV is resonant with  $S_2$ , all trajectories started in the electronic state  $S_2$ . The

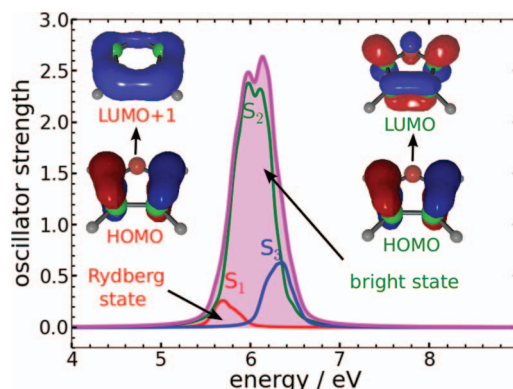


FIG. 1. Theoretical absorption spectrum of furan at 300 K. The absorption for individual excited states is shown in red for  $S_1$ , green for  $S_2$  and blue for  $S_3$ . The total absorption spectrum is depicted by the filled magenta curve. The discrete absorption lines for all initial geometries were convolved with a Lorentzian of width 0.1 eV and summed. The insets show the orbitals for the dominant excitations of  $S_1$  (left) and  $S_2$  (right). At the optimized (PBE0/6-311++G\*\*) equilibrium geometry  $S_1$  is a dark Rydberg state (HOMO  $\rightarrow$  LUMO+1 excitation,  $\epsilon_1 = 5.87$  eV) while  $S_2$  is the bright state (HOMO  $\rightarrow$  LUMO excitation,  $\epsilon_2 = 6.21$  eV).

energy spectrum of the pump pulse also overlaps with the Rydberg state  $S_1$ , but the oscillator strength is much smaller than for  $S_2$ . We started additional 10 trajectories on  $S_1$  and found that by neglecting a small initial population on this state we do not miss any feature in the theoretical anisotropy map. During the simulation the Rydberg state is reached through decay from  $S_2$ . Since the ground state cannot be ionized by the experimental probe pulse of 4.8 eV, the photoionization spectrum is exclusively due to trajectories on the states  $S_1$  and  $S_2$ .

## 2. Selection of Dyson orbitals

We selected those Dyson orbitals that are relevant to the experiment reasoning as follows: With a probe energy of 4.8 eV, molecules in the ground state cannot be ionized. Ionization from the neutral ground state to the cationic ground state already requires 9 eV at equilibrium geometry and is, therefore, unlikely to be energetically possible at any other geometry reached during the simulation. As  $S_1$  and  $S_2$  can be ionized to the lowest three cation states  $D_0$ ,  $D_1$ , and  $D_2$ , the Dyson orbitals for the transitions  $S_1$ ,  $S_2 \rightarrow D_0$ ,  $D_1$ ,  $D_2$  are needed. Since the ionization energies for the transitions  $S_1 \rightarrow D_0$ ,  $S_2 \rightarrow D_0$ ,  $S_1 \rightarrow D_1$ , and  $S_2 \rightarrow D_1$  are overestimated at PBE0/6-311++G\*\* level by  $\approx 1$  eV as compared with EOMCCSD/6-311G\*\*(3df)<sup>41,42</sup> at the equilibrium geometry, the ionization energies for these channels are shifted down by 1 eV.

## 3. Simulation procedure

The non-adiabatic dynamics has been performed in the frame of TDDFT as described previously.<sup>17</sup> The energies and

gradients needed for integrating Newton's equations of motion as well as the non-adiabatic couplings needed for determining the surface hopping probabilities were calculated "on the fly" in the frame of TDDFT. The time step for the propagation of the nuclear trajectories was 0.1 fs. At each nuclear time step the electronic Schrödinger equation was integrated with a time step of  $10^{-6}$  fs.

The trajectories were propagated for 200 fs which is enough to observe the ultrafast decay from  $S_2$  to  $S_1$  and the slightly slower decay from  $S_1$  to the electronic ground state. The electronic structure of the neutral molecule ( $N$  electrons) and the ionized molecule ( $N-1$  electrons) at the same geometry were calculated at intervals of 1 fs along each trajectory using TDDFT. Energies and wave functions (linear combinations of single excitation from the Kohn-Sham reference state) for the 3 lowest excited neutral states and ionized states were extracted from linear response TDDFT calculations performed with the Turbomole package.<sup>35</sup> From the overlap of the neutral wave function of the current state with the cation ground state wave functions Dyson orbitals were obtained along each trajectory (using Eq. (20) to reduce the overlap between neutral and cation Slater determinants). In order to calculate orientation averaged transition dipole matrix elements the Dyson orbitals were shifted by their dipole moments and expanded into spherical harmonics on a Lebedev grid.<sup>36</sup> Spherical wave components for Coulomb waves (Eq. (27)) were computed on the same radial grid for a range of photoelectron kinetic energies. For each trajectory  $i$ , maps for  $\sigma_i(\text{PKE}, t)$  and  $\beta_i(\text{PKE}, t)$  were calculated using the Dyson orbital at time  $t$  as initial state and Coulomb waves for an electron with momentum  $k = \sqrt{2\text{PKE}}$  as final states.

In order to calculate the anisotropy parameter along one non-adiabatic trajectory we calculated the transition dipole

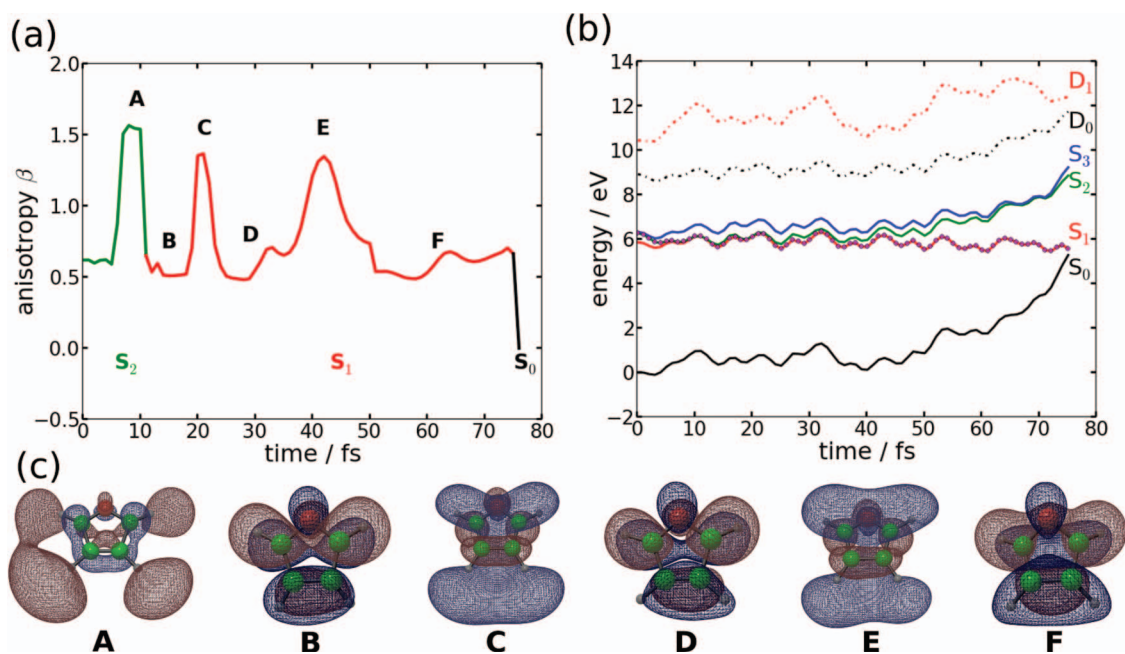


FIG. 2. Anisotropies (a), energy levels (b), and Dyson orbitals (c) along a typical trajectory. (a) After a fast decay from  $S_2$  to  $S_1$  the Dyson orbital oscillates between an extended s-like orbital with high anisotropy (C and E) and a valence orbital with lower anisotropy (B, D, and F). On transition to the ground state the anisotropy drops drastically. (b) The current state is marked by magenta dots. Non-adiabatic transitions occur after less than 10 fs from  $S_2$  to  $S_1$  and after 75 fs from  $S_1$  to the ground state.

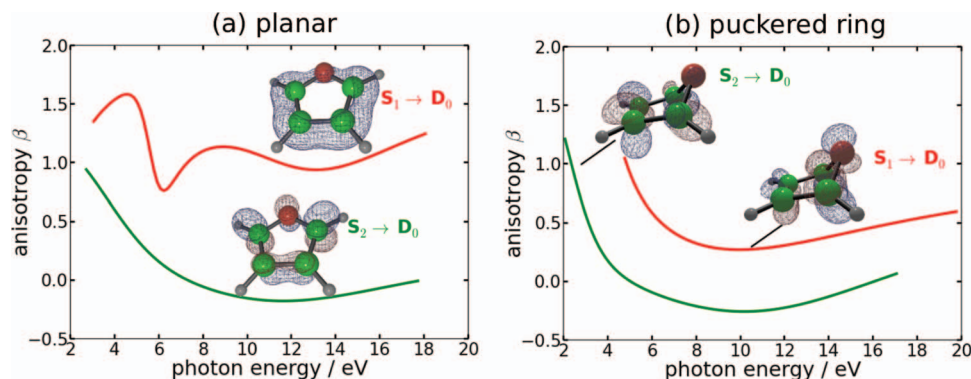


FIG. 3. Anisotropies at key geometries. Anisotropy parameters depend strongly on the nuclear geometry and the electronic state. (a) The planar equilibrium geometry shows a high positive anisotropy for  $S_1$  over the entire photon energy range typical of an s-type orbital. At the ring puckering conical intersection (b) both states acquire valence character. Cross sections were averaged isotropically.

moment  $\vec{d}_{0 \rightarrow I} = (d_x, d_y, d_z)$  between the ground state and the excited state  $I$  in the first time step, i.e., at the time of the pump pulse. The photoionization cross section was then averaged over molecular orientations with the  $\frac{3}{2} \cos^2(\beta - \Theta)$  weight factor, where  $\Theta = \arccos(\frac{d_z}{|\vec{d}|})$ .

Finally, the maps of all trajectories were combined. Each trajectory contributes only along a line where energy conservation  $h\nu = \text{PKE} + \text{IE}(t)$  is satisfied ( $\nu$  is the frequency of the probe pulse and  $\text{IE}(t)$  the energy difference between the current neutral state and the cation ground state along the trajectory). For points in  $(\text{PKE}, t)$ -space that were visited by more than one trajectory, the averaged anisotropy parameter is obtained as  $\beta(\text{PKE}, t) = (\sum_i \sigma_i(\text{PKE}, t) \beta_i(\text{PKE}, t)) / (\sum_i \sigma_i(\text{PKE}, t))$ .

## B. Results and discussion

The electronic excitation to the  $S_2$  state leads to an ultrafast population decay with the time constants  $\tau(S_2 \rightarrow S_1) \approx 10$  fs and  $\tau(S_1 \rightarrow S_0) \approx 50$  fs. One typical non-adiabatic trajectory is shown in Fig. 2.

Whereas the first and second excited states are very close in energy (see Fig. 2(b)), so that non-adiabatic transitions between them can happen at any time shortly after the excitation, the relaxation to the ground state occurs later through different conical intersections.<sup>1</sup> One is associated with an out-of-plane movement of the oxygen. Another relaxation mechanism is accompanied by an opening of the ring at the oxygen atom. These geometries were identified in Ref. 37 in the framework of the MS-CASPT2/6-311G\* method. We find in

our TDDFT simulation that the transitions occur close to similar geometries.

The change in the character of the Dyson orbital can be read off directly from the anisotropy parameters, as the nuclear geometry changes from planar to ring-puckered (compare Fig. 3(a) with Fig. 3(b)). At planar geometry it is positive over the entire energy range for ionization from  $S_1$ , as expected from an s-orbital. For ionization from  $S_2$  it is negative and has a dip at low PKE, which is a sign of a p- or d-orbital. At the conical intersection both Dyson orbitals show the anisotropy profile characteristic of a valence orbital.

Anisotropies do not remain constant in one electronic state. Vibrations on  $S_1$  can cause the Dyson orbital to expand into a Rydberg-like orbital and to contract again periodically into a valence orbital, as was found by analyzing the excited state character previously.<sup>1</sup> A plot of the anisotropy parameters along a typical trajectories shows peaks and troughs when the Dyson orbital cycles between the two shapes (Fig. 2(a)). The transition to the ground state leads to a fast increase in the ionization potential and a decrease in the anisotropy parameter.

In Fig. 4, the simulated photoionization cross section map is compared with the experimental one. The map was produced by superimposing the photoionization cross sections for the included ionization channels  $S_1, S_2 \rightarrow D_1, D_2$  along 189 non-adiabatic trajectories and averaging appropriately for  $(\text{PKE}, t)$ -points that are crossed by more than one trajectory. The  $(\text{PKE}, t)$  coordinates of individual trajectories are determined by the condition that the kinetic energy of the photoelectron and the ionization potential of the channel  $N \rightarrow I$  have to add up to the photon energy,  $h\nu = \text{PKE} + \text{IE}_{N \rightarrow I}(t)$ .

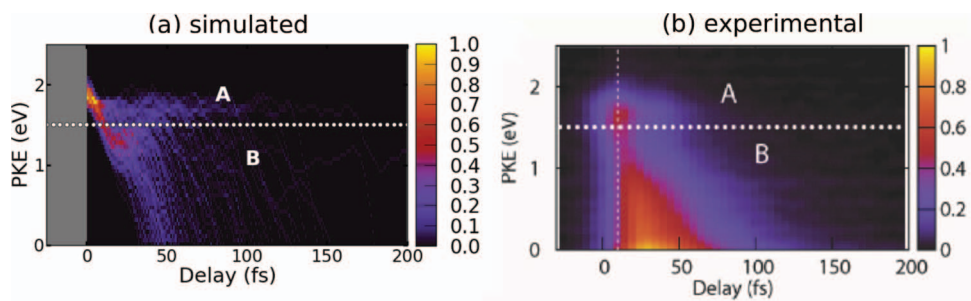


FIG. 4. Simulated (a) and experimental<sup>1</sup> (b) photoionization cross section maps of furan.



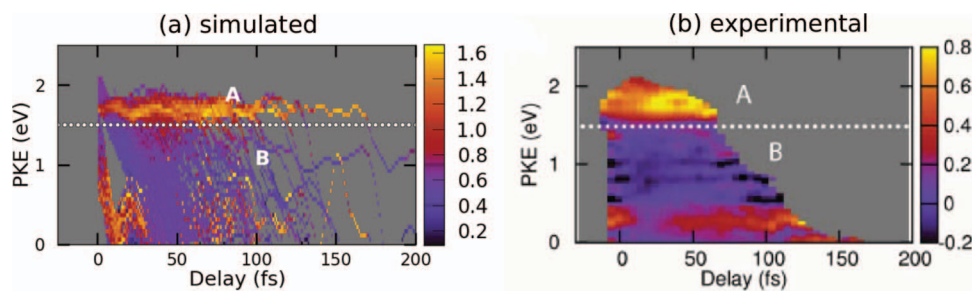


FIG. 5. Simulated (a) and experimental<sup>1</sup> (b) anisotropy maps of furan. The electronic character of the initially pumped state changes from a Rydberg state with high anisotropy in region A to a valence state with lower anisotropy in region B. In the simulated map the anisotropies along 189 trajectories are superimposed. Final continuum states of the electron were modelled by Coulomb waves. The same colormap is used for both plots: Although the absolute values differ (simulated anisotropies are higher by 0.8), the relative changes between components A and B agree (from 0.8 to  $-0.2$  in the experiment and from 1.6 to 0.6 in the simulation).

The simulated cross section map shows the clearly visible Rydberg state (component A at 1.8 eV) which is separated from the low-PKE signal. Although the strong signal at low PKE is missing in the simulated map, the envelope of the signal agrees with the experiment. The strong signal at low PKE comes from the rearrangement of the nuclear wave packet as it interacts with the probe pulse. We could reproduce it in previous work<sup>1</sup> by assuming constant Franck-Condon factors.

In Fig. 5, simulated and experimental maps of the anisotropy are shown. Analyzing the anisotropy map by ionization channels reveals that the features at PKE  $\approx 1.8$  eV stem from ionization to  $D_0$  while the signal at PKE  $\approx 0.4$  eV comes from ionization to  $D_1$ . Overall the simulated anisotropy map nicely reproduces the most important experimental features. Both maps exhibit positive anisotropy values in the region which is associated with ionization from the Rydberg state to  $D_0$ . This region is separated by an area of low anisotropy, which is characteristic for ionization from a valence state, from the low PKE-region below 1 eV, which is attributed to ionization to  $D_1$ . The disappearance of the high anisotropy around 25 fs in the region can be linked to the oscillations in the ionization potential due to vibration within the furan ring. It should be pointed out that the  $D_1$ -channel is weak and cannot be seen in the map of the cross section (Fig. 4), but it can be seen in the anisotropy map (Fig. 5), which is independent of absolute intensities. This demonstrates the strength of the TRPEI method.

Although our simulation overestimates the absolute anisotropy values, the separation between the two regions and the relative changes are reproduced quantitatively correctly. Notice that the convolution of the simulated anisotropy map with the experimental probe pulse in the energy and time domain could in principle lower these values. However, in order to perform this convolution values for (PKE,  $t$ )-points, which are not crossed by trajectories, would have to be assigned arbitrarily.

The main limitations of the method are the use of Coulomb waves as continuum states and the neglect of Franck-Condon factors for the ionization transition. While the Dyson orbital accounts for the correct molecular geometry and for rearrangements of the electronic structure in the ion, the final states are oblivious to both relaxation effects and the shape of the molecule. In the TRPEI experiment on

furan, the signal at high photoelectron kinetic energy was attributed to photoionization from a Rydberg state. According to the Cooper-Zare formula<sup>38</sup> the anisotropy should be close to 2, but the experiment shows much lower values around 0.6. Although the Dyson orbital resembles an s-orbital, the continuum states to which the electron is ionized do not have spherical symmetry. Therefore, Coulomb functions as final states cannot lead to quantitative predictions for anisotropy parameters. Better agreement with the experiment should be achieved by using molecular scattering states as final states, but as already mentioned they are notoriously complicated to calculate. Notice that another source of error might be the Gaussian basis set used to expand the Dyson orbital. Photoelectron angular distributions have been shown by Oana<sup>19</sup> to be sensitive to the diffuse tails of the Dyson orbitals, which cannot be accurately described by quickly decaying Gaussians. This note might be particularly relevant to diffuse extended Rydberg states. Our choice of the basis set, which includes diffuse functions, has been previously shown to reproduce correctly the energetic position of the Rydberg state as well as main features of the photoionization signal.<sup>1</sup>

The second shortcoming is related to the treatment of the nuclear wave functions and their interaction with the laser field. The probe pulse can interact with the nuclear wave packet and redistribute vibrational energy. This effect could be accounted for with the field-induced surface hopping method.<sup>18</sup> The description of the nuclear wave function could be improved by replacing point-like classical trajectories by interacting swarms of parametrized wave-packets as in the *ab initio* multiple spawning method, which has been used recently to calculate photoelectron spectra for benzene.<sup>39</sup>

#### IV. CONCLUSION AND OUTLOOK

We have presented a method for simulating time-resolved photoelectron imaging spectra based on trajectory surface hopping non-adiabatic dynamics. The method is efficient and generally applicable to complex polyatomic molecules and can serve for the interpretation of TRPEI experiments providing valuable insight into the photochemistry and photo-physics.

Non-adiabatic dynamics is modelled by propagating a swarm of trajectories that can jump between different

electronic states. For each delay time along a non-adiabatic trajectory, photoionization by the probe pulse is treated as an instantaneous transition from the Dyson orbital between the current state and the cation ground state to the electronic continuum, which is approximated by Coulomb waves orthogonalized with respect to the Dyson orbital. Anisotropy parameters of the photoelectron angular distribution are obtained from averaging the transitions dipole moments between the Dyson orbitals and Coulomb waves over molecular orientations analytically. By averaging over all trajectories we can produce time- and energy-resolved maps of the total cross section  $\sigma$  and the anisotropy  $\beta$ , which can be directly compared to experimental data.

We have applied our method to the furan molecule for which experimental data are available from our previous work.<sup>1</sup> Our simulations have allowed us to interpret the experimental TRPEI spectrum by assigning the experimental features to the underlying dynamics involving valence and Rydberg excited states.

The interpretation of TRPEI experiments remains challenging if the underlying dynamics are not accompanied by clear signatures in the photoelectron kinetic energy spectrum such as a Rydberg state. Experiments where the changes of the photoelectron angular distribution are more subtle require a joint theory of molecular dynamics and photoionization. Our work represents a step in this direction. Further improvements will include a better description of the electronic continuum that treats photoionization beyond Fermi's golden rule and takes into account the impact of the pump and probe pulses on the nuclear dynamics. Such a theory could then be expanded to treat shaped laser pulses that steer coupled nuclear and electronic dynamics in a controllable fashion.

## ACKNOWLEDGMENTS

A.H. and R.M. acknowledge financial support by the Deutsche Forschungsgemeinschaft (DFG) within the priority program "Ultrafast Nanooptics" (SPP 1391). Furthermore, M.W. and R.M. acknowledge funding within the DFG Emmy-Noether Program (MI-1236). A.H. also acknowledges funding by his parents.

<sup>1</sup>T. Fuji, Y.-I. Suzuki, T. Horio, T. Suzuki, R. Mitrić, U. Werner, and V. Bonačić-Koutecký, *J. Chem. Phys.* **133**, 234303 (2010).

<sup>2</sup>J. Michl and V. Bonačić-Koutecký, *Electronic Aspects of Organic Photochemistry* (Wiley, 1990).

<sup>3</sup>D. Polli, P. Altoe, O. Weingart, K. Spillane, C. Manzoni, D. Brida, G. Tomasello, G. Orlandi, P. Kukura, R. Mathies, M. Garavelli, and G. Cerullo, *Nature (London)* **467**, 440 (2010).

<sup>4</sup>T. Gustavsson, R. Improta, and D. Markovitsi, *J. Phys. Chem. Lett.* **1**, 2025 (2010).

<sup>5</sup>T. Suzuki, *Annu. Rev. Phys. Chem.* **57**, 555 (2006).

<sup>6</sup>A. Stolow and J. Underwood, *Adv. Chem. Phys.* **139**, 497 (2008).

<sup>7</sup>G. Wu, P. Hockett, and A. Stolow, *Phys. Chem. Chem. Phys.* **13**, 18447 (2011).

<sup>8</sup>T. Suzuki, *Int. Rev. Phys. Chem.* **31**, 265 (2012).

<sup>9</sup>T. Horio, T. Fuji, Y.-I. Suzuki, and T. Suzuki, *J. Am. Chem. Soc.* **131**, 10392 (2009).

<sup>10</sup>Y.-I. Suzuki, T. Fuji, T. Horio, and T. Suzuki, *J. Chem. Phys.* **132**, 174302 (2010).

<sup>11</sup>Y.-I. Suzuki, T. Horio, T. Fuji, and T. Suzuki, *J. Chem. Phys.* **134**, 184313 (2011).

<sup>12</sup>R. Lucchese, K. Takatsuka, and V. McKoy, *Phys. Rep.* **131**, 147 (1986).

<sup>13</sup>Y. Arasaki, K. Takatsuka, K. Wang, and V. McKoy, *J. Chem. Phys.* **132**, 124307 (2010).

<sup>14</sup>H. R. Hudock and T. J. Martinez, *ChemPhysChem* **9**, 2486 (2008).

<sup>15</sup>H. Tao, T. K. Allison, T. W. Wright, A. M. Stooke, C. Khurmi, J. van Tilborg, Y. Liu, R. W. Falcone, A. Belkacem, and T. J. Martinez, *J. Chem. Phys.* **134**, 244306 (2011).

<sup>16</sup>R. Mitrić, U. Werner, and V. Bonačić-Koutecký, *J. Chem. Phys.* **129**, 164118 (2008).

<sup>17</sup>R. Mitrić, J. Petersen, M. Wohlgenuth, U. Werner, V. Bonačić-Koutecký, L. Wöste, and J. Jortner, *J. Phys. Chem. A* **115**, 3755 (2011).

<sup>18</sup>R. Mitrić, J. Petersen, and V. Bonačić-Koutecký, *Phys. Rev. A* **79**, 053416 (2009).

<sup>19</sup>C. Oana and A. Krylov, *J. Chem. Phys.* **131**, 124114 (2009).

<sup>20</sup>J. Sakurai, *Modern Quantum Mechanics* (Addison-Wesley, 1994).

<sup>21</sup>M. Walter and H. Häkkinen, *New J. Phys.* **10**, 043018 (2008).

<sup>22</sup>C. Oana and A. Krylov, *J. Chem. Phys.* **127**, 234106 (2007).

<sup>23</sup>K. Reid, *Annu. Rev. Phys. Chem.* **54**, 397 (2003).

<sup>24</sup>A. Edmonds, *Angular Momentum in Quantum Mechanics* (Princeton University Press, 1957).

<sup>25</sup>B. Ritchie, *Phys. Rev. A* **13**, 1411 (1976).

<sup>26</sup>ezDyson v2, manual of the program developed by Krylov *et al.*, available at <http://iopenshell.usc.edu/downloads/ezdyson/>.

<sup>27</sup>M. Casida, *Recent Advances in Density Functional Methods*, edited by D. Chong (World Scientific, 1995).

<sup>28</sup>M. Le Bellac, *Quantum Physics* (Cambridge University Press, 2006).

<sup>29</sup>M. Abramowitz and I. Stegun, *Handbook of Mathematical Functions* (Dover, 1965).

<sup>30</sup>W. Press, S. Teukolsky, W. Vetterling, and B. Flannery, *Numerical Recipes in C* (Cambridge University Press, 1999).

<sup>31</sup>H. Bethe and E. Salpeter, *Quantum Mechanics of One- and Two-Electron Atoms* (Springer, 1957).

<sup>32</sup>A. Messiah, *Quantum Mechanics* (Dover, 1999).

<sup>33</sup>C. Adamo and V. Barone, *J. Chem. Phys.* **110**, 6158 (1999).

<sup>34</sup>R. Krishnan, J. Binkley, R. Seeger, and J. Pople, *J. Chem. Phys.* **72**, 650 (1980).

<sup>35</sup>TURBOMOLE V6.4 2012, a development of University of Karlsruhe and Forschungszentrum Karlsruhe GmbH, 1989–2007, TURBOMOLE GmbH, since 2007; available at <http://www.turbomole.com>.

<sup>36</sup>V. Lebedev, *USSR Comput. Math. Math. Phys.* **15**, 44 (1975).

<sup>37</sup>M. Stenrup and Å. Larson, *Chem. Phys.* **379**, 6 (2011).

<sup>38</sup>J. Cooper and R. N. Zare, *J. Chem. Phys.* **48**, 942 (1968).

<sup>39</sup>A. Thompson and T. Martinez, *Faraday Discuss.* **150**, 293 (2011).

<sup>40</sup>Y.-I. Suzuki and T. Suzuki, *J. Phys. Chem. A* **112**, 402–411 (2008).

<sup>41</sup>J. F. Stanton and R. J. Bartlett, *J. Chem. Phys.* **98**, 7029 (1993).

<sup>42</sup>M. J. Frisch, G. W. Trucks, H. B. Schlegel *et al.*, Gaussian 09, Revision A.02, Gaussian, Inc., Wallingford, CT, 2009.